The Planetary Science Journal, 7:65 (13pp), 2026 March https://doi.org/10.3847/PSJ/ae4749

Space Weathering Age of Itokawa and Eros by Machine Learning

Lakshika Palamakumbure[1], David Korda[2], and Tomáš Kohout[3,4,5]
[1] Department of Geosciences and Geography, University of Helsinki, Finland
[2] Astronomical Institute of the Czech Academy of Sciences, Czech Republic
[3] Department of Physics and Astronomy, University of Turku, Finland
[4] School of Electrical Engineering, Aalto University, Finland
[5] Institute of Geology of the Czech Academy of Sciences, Czech Republic
Received 2025 November 3; revised 2026 February 5; accepted 2026 February 16; published 2026 March 17

Abstract

Near-Earth asteroids such as Itokawa and Eros provide valuable insights into the collisional and surface evolution of the inner solar system. As S-type asteroids, their surfaces are altered by space weathering (SW) from solar wind and micrometeorite impacts. Because SW progresses over time, it serves as a proxy for estimating surface exposure ages, revealing resurfacing and geologic histories. This study estimates the SW ages at the present conditions of Itokawa and Eros using a machine learning model developed by L. Palamakumbure et al. The ensemble model was trained on laboratory reflectance spectra of irradiated silicate samples (olivine, pyroxene, mixtures, and chondrites) to capture spectral changes due to SW. Asteroid spectra were obtained from the Near Infrared Spectrometer (Hayabusa) dataset for Itokawa and the Near-Infrared Spectrometer (NEAR Shoemaker) dataset for Eros via NASA Planetary Data System. SW ages for Itokawa range from 1.9 kyr to 2.5 Gyr, reflecting alteration from both solar wind and micrometeorite impacts. Eros, in contrast, shows older SW ages (0.4 to 2 Gyr), dominated by micrometeorite effects. These results align with previous studies and Hayabusa sample analyses, confirming Itokawa's young surfaces are influenced by solar wind, with older, less disturbed regions such as Arcoona. Eros displays more uniformly mature surfaces, with localized relatively young areas linked to cratering or regolith movement. The contrasting SW ages highlight how asteroid size, regolith behavior, and orbital characteristics influence SW processes. Overall, the study demonstrates the potential of machine learning for reconstructing surface exposure histories on airless bodies.

Unified Astronomy Thesaurus concepts: Small Solar System bodies (1469); Near-Earth objects (1092); Asteroids (72); Eros (2182); Asteroid surfaces (2209)

1. Introduction

Asteroids in the solar system undergo breakup or collision events, which shape their surfaces and are fundamental in the broader dynamical evolution of the system. Among these, S-type asteroids dominate the inner asteroid belt (R. P. Binzel et al. 2004; T. L. Dunn et al. 2013; F. E. DeMeo & B. Carry 2014) and are particularly important as they may preserve a record of the abovementioned events within their regolith layers.

Space weathering (SW) on asteroids refers to the progressive alteration of surface materials due to exposure to the space environment. These processes induce changes in spectral properties, such as reddening and darkening of reflectance spectra, and can modify absorption band parameters associated with olivine (OL) and pyroxene minerals. Due to SW, reflectance spectra of S-type asteroids typically exhibit progressive spectral reddening, decrease in albedo, and reduction in mineral absorption band strength (e.g., G. Strazzulla et al. 2005; R. Brunetto et al. 2006; Z. Kanuchova et al. 2015; L. Palamakumbure et al. 2023; Y. Zhuang et al. 2023). Laboratory simulations have confirmed that these spectral changes are diagnostic of SW processes (e.g., S. Marchi et al. 2005; G. Strazzulla et al. 2005; R. Brunetto et al. 2006; T. Kohout et al. 2020; K. Chrbolková et al. 2022; L. Palamakumbure et al. 2023), enabling remote sensing techniques to infer surface maturity. Early studies using Sloan Digital Sky Survey data established a correlation between asteroid age and spectral reddening, with initial SW timescales of ≈1 Gyr (R. Jedicke et al. 2004). Subsequent analyses of spectral slopes in main-belt asteroids refined this relationship, suggesting a logarithmic evolution of spectral features with age and revising the SW timescale to ≈570 Myr (D. Nesvorný et al. 2005; M. Willman et al. 2008, 2010; M. Willman & R. Jedicke 2011). More recent work by P. Vernazza et al. (2009) reconciled previous discrepancies, helping to unify SW models with dynamical constraints.

An impact event on an asteroid typically excavates a fresh surface, and through its exposure to the interplanetary environment, a new cycle of SW is initiated. Over time, this fresh regolith is progressively altered by three primary SW agents: micrometeorite impacts, solar wind irradiation, and Galactic irradiation. Because SW effects accumulate with time, they serve as useful proxy indicators for estimating the SW age of an asteroid following a collision or resurfacing event (e.g., D. Nesvorný & W. F. Bottke 2004; R. Brunetto et al. 2006; L. Palamakumbure et al. 2025). In turn, determining asteroid SW ages aids in understanding the chronology of the solar system.

The SW age distribution of individual asteroids can vary due to several factors, including their size, surface dynamics, ongoing regolith evolution, resurfacing processes, and repeated collisional events (C. R. Chapman 2004; T. Hiroi et al. 2006;

M. Ishiguro et al. 2007; S. C. Koga et al. 2018; F. E. DeMeo et al. 2023). However, for most S-type asteroids, full coverage of the spatially resolved reflectance data across their entire surfaces is not available, limiting our ability to assess these variations. Notably, only two S-type asteroids, namely, (25143) Itokawa and (433) Eros, have been extensively studied through direct spacecraft observations. The Hayabusa mission provided high-resolution data on Itokawa (J. Kawaguchi et al. 2003), while NEAR Shoemaker conducted a comprehensive survey of Eros (A. F. Cheng 1997). These missions offer rare and valuable insights into the complex surface histories and compositional diversity of S-type asteroids.

Itokawa is a small, elongated asteroid with approximate dimensions of $0.5 \times 0.29 \times 0.20$ km (H. Demura et al. 2006). It is believed to be a rubble-pile body formed through a contact binary origin, as suggested by observations from the Hayabusa mission (A. Fujiwara et al. 2006). Several studies have provided evidence of minor-to-moderate SW on Itokawa through a range of analyses, including albedo variations (J. Saito et al. 2006), SW coefficient assessments (M. Ishiguro et al. 2007), principal component analysis (S. C. Koga et al. 2018), compositional and SW analysis (D. Korda et al. 2023), and boulder surface studies using AMICA images (S. Jin & M. Ishiguro 2022).

The strongest evidence for SW on Itokawa comes from laboratory analyses of samples returned by the Hayabusa mission. These grains exhibit clear signs of SW, including amorphous rims with nanophase metallic iron particles ($npFe^0$) and iron sulfide nanoparticles (npFeS), rims with anomalous chemical compositions, metallic iron whiskers on troilite surfaces, and vesicles (T. Noguchi et al. 2011, 2014; L. P. Keller & E. L. Berger 2014; M. S. Thompson et al. 2014a; T. Matsumoto et al. 2015; K. D. Burgess & R. M. Stroud 2021). T. Noguchi et al. (2014) estimated the SW age of Itokawa to be between 10^3 and 10^4 yr, identifying solar wind irradiation as the dominant weathering mechanism. This conclusion was further supported by studies from L. P. Keller & E. L. Berger (2014), M. S. Thompson et al. (2014a), and T. Matsumoto et al. (2015). Moreover, K. D. Burgess & R. M. Stroud (2021) observed differing degrees of weathering in two sampling sites within the same region, suggesting that SW on Itokawa is spatially heterogeneous, even at relatively small scales.

In contrast, Eros is a monolithic elongated asteroid with an approximate dimension of $34.4 \times 11.2 \times 11.2$ km. Its surface appears compositionally homogeneous, with only a subtle spectral variation observed across its northern hemisphere (L. A. McFadden et al. 2001; L. R. Nittler et al. 2001; J. Bell et al. 2002; D. Korda et al. 2023). These minor spectral differences are often associated with steep slopes, large impact craters, and surface protrusions. Specifically, weak variations in band-area ratios have been reported between the major impact craters Psyche and Himeros (J. Bell et al. 2002). B. E. Clark et al. (2001) argued that the spectral variation on Eros is influenced not only by differences in mineralogy and grain size but also by SW processes, which contribute to optical maturity. Furthermore, the low sulfur content observed on Eros's surface has been linked to solar wind–induced SW (A. Kracher & D. W. Sears 2005), which may have preferentially depleted FeS from the uppermost regolith due to its low dissociation energy.

Although prior studies have established the presence of SW in both Itokawa and Eros and provided broad SW age estimates, these are often averaged across the entire surface. Our study seeks to improve upon this by determining spatially resolved SW age and identifying the dominant SW mechanisms for both asteroids. Here, SW age is defined as the time an asteroid has been exposed to an interplanetary environment after a breakup from a parent body or after a resurfacing event. In this study, we determine SW age under present-day interplanetary environmental conditions and at the current asteroid heliocentric distance. We note that the heliocentric distance and planetary environments experienced by asteroids evolve over time, creating a level of uncertainty between our SW age and real surface exposure age, as discussed in detail in Section 5.3. We employ a machine learning model developed by L. Palamakumbure et al. (2025) trained with legacy SW laboratory experiment reflectance data, outputting the absolute SW age. By applying this model to high-resolution spectral observations of Itokawa and Eros, we aim to generate detailed SW age maps, evaluate spatial variability in SW, and refine our understanding of regolith evolution and asteroid surface processes. These insights will not only enhance current models of asteroid aging but also support future mission planning.

2. Data Collection and Processing

2.1. Training Data

To adapt the model developed by L. Palamakumbure et al. (2025) for our analysis, we retrained and validated it using the same dataset employed in the original study. However, we modified the spectral preprocessing steps to better align with the characteristics (e.g., spectral range) of the reflectance data available for Itokawa and Eros. In this implementation, reflectance spectra and irradiation type were used as independent variables, while the exposure time at 1 au served as the dependent variable, consistent with the original framework.

The training dataset contains the 169 reflectance spectra of OL, orthopyroxene (OPX), OL-OPX mixtures, and ordinary chondrite (OC) samples irradiated using H^+ and laser. We normalized the reflectance at 1500 nm for Itokawa, approximately midway between the two absorption bands. For Eros, normalization was performed at 1300 nm due to excessive reddening, where the germanium detector provides more reliable measurements (J. Veverka et al. 2000). These adjustments ensured compatibility between the model inputs and the spectral ranges of the Itokawa and Eros datasets. Subsequent denoising and interpolation were carried out as described below, following the methodology of D. Korda et al. (2023).

To reduce noise in the spectral data, a Gaussian smoothing filter was employed. The filter's standard deviation, set to 7 nm in this study, was chosen based on the spectral resolution to ensure optimal smoothing without compromising spectral features. To correct for edge effects caused by the filtering, we applied the same Gaussian filters to an array of ones that had the same length as the wavelength grid. The smoothed spectral data were then divided by this correction factor, preserving the overall spectral shape while minimizing boundary distortions.

Using the cubic interpolation, the reflectance spectra were interpolated to a uniform range of 820–2080 nm and 820–2360 nm with 20 nm intervals. The interpolation function

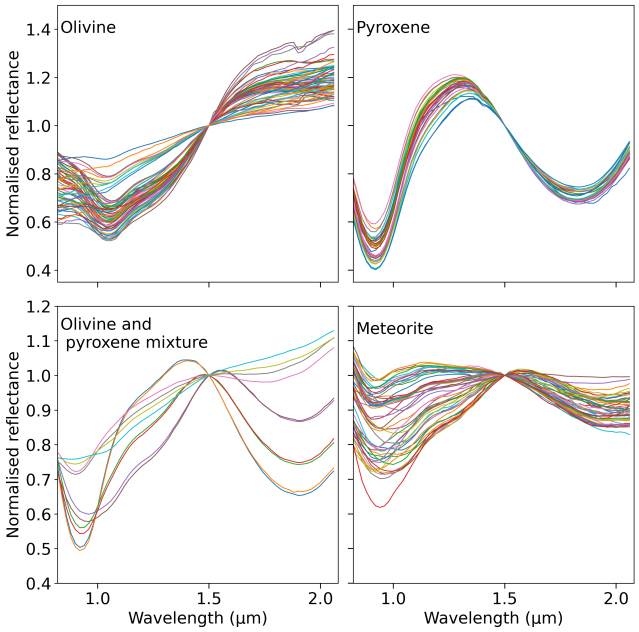

Figure 1. Denoised and normalized spectra of silicate minerals, mixtures, and meteorite samples. All spectra are renormalized at 1500 nm.

was constructed from the denoised spectral data and the corresponding wavelength values using

$$f(\lambda) = \text{interp1d}(\lambda, R_{\text{denoised}}, \text{kind}=\text{“cubic”}), \quad (1)$$

where R_{denoised} represents the denoised reflectance values. Interpolation was performed using the “interp1d” function from the “scipy.interpolate” module. To identify the relative difference between the spectra and remove absolute albedo information, we normalized the spectra as shown in Figure 1. The interpolated values at λ_{norm} (in this study, $\lambda_{\text{norm}} = 1500$ nm for Itokawa and 1300 nm for Eros) were used to normalize the entire spectrum as follows:

$$R_{\text{normalized}} = \frac{R_{\text{denoised}}}{f(\lambda_{\text{norm}})}. \quad (2)$$

2.2. Reflectance Spectra of Itokawa and Eros

The reflectance spectra used in this study were obtained from the Near-Infrared Spectrometer (NIS) on board NEAR Shoemaker for Eros (J. W. Warren et al. 1997) and the Near Infrared Spectrometer (NIRS) on board Hayabusa for Itokawa (M. Abe et al. 2011), both retrieved from the NASA Planetary Data System. Specifically, we used the EAR_A_NIS_5_EDR_ALL_PHASES_PDSREV_V1_0 dataset for Eros and the HAY_A_NIRS_3_NIRSCAL_V1_0 dataset for Itokawa. The NIS on board the NEAR Shoemaker spacecraft acquired more than 200,000 spatially resolved reflectance spectra of asteroid Eros over the 800–2500 nm wavelength range. A key subset of approximately 2000 spectra, known as the low-phase flyby dataset, was collected at phase angles of 1°–47°, providing observations of the northern hemisphere at spatial resolutions ranging from 6 × 12 to 1.25 × 2.5 km per spectrum (J. Bell et al. 2002). During the Hayabusa rendezvous with asteroid Itokawa, the spacecraft's NIRS acquired a large set of reflectance spectra of the asteroid's surface. The NIRS instrument operated over an effective wavelength range of 850–2100 nm, capturing absorption features of OL and OPX typical of S-type asteroids. This dataset includes over 80,000 spatially resolved spectra covering most of Itokawa's surface, obtained at phase angles from approximately 0° to 38° and spatial footprints ranging roughly from 6 to 90 m^2 per spectrum (C. Ni & H. Zhang 2025). Both datasets include basic dark-frame and/or dark-current corrections, as well as illumination-geometry corrections required to convert the raw data to radiance factor (I/F) reflectance units. To obtain a coherent dataset, the spectra were preprocessed following the methodology described in D. Korda et al. (2023).

Table 1
Selection Criteria, Number of Spectra, and Final Wavelength Grid for Itokawa and Eros

	Itokawa		Eros	
Parameter	Min	Max	Min	Max
Phase angle (deg)	0	30	0	40
Incidence angle (deg)	0	50	0	60
Emission angle (deg)	0	50	0	60
Observed angle (deg^2)	⋯	⋯	0	750
Distance from the surface (km)	0	5		
Wavelength grid (nm)	820	2080	820	2360
Wavelength spacing (nm)	20		20	
Normalized at (nm)	1500		1300	
# Raw reflectance	8358		1684	
# Reflectance	18695		15353	

The data were filtered according to the selection criteria given in Table 1. Unreliable spectra, including those with very low or negative reflectance values, were removed. For Itokawa, spectra with reflectance values below 800 nm were excluded due to known instrumental bias (D. Korda et al. 2023). After this selection process, a total of 8358 raw reflectance spectra for Itokawa and 1684 for Eros were retained for this study.

Because of the varying spectrometer footprint and spatial overlap depending on the distance and observation geometry, the asteroid surfaces were divided into uniform 1° × 1° latitude–longitude target regions. For each region, a representative spectrum was obtained by computing a weighted average of all spectra overlapping that region, with weights proportional to the overlap area relative to the total footprint. This procedure results in spectral coverage for approximately 35% of Eros and 45% of Itokawa surfaces. The averaged spectra were subsequently denoised using a Gaussian convolution kernel and renormalized as described in Section 2.1. For Eros, an additional red-slope correction was applied to account for known calibration issues above 1500 nm in the NIS spectra, based on a comparison with ground-based observations of F. E. DeMeo et al. (2023). In addition, spectra of Eros were normalized at 1300 nm due to extensive reddening, where the germanium detector provides more reliable data (J. Veverka et al. 2000). After preprocessing the data, 18,695 and 15,353 reflective spectra were obtained for Itokawa and Eros, respectively.

3. Methods

3.1. Model Training and Validation

The Ensemble model developed by L. Palamakumbure et al. (2025) combines five machine learning algorithms: a convolutional neural network (CNN), gradient boosting

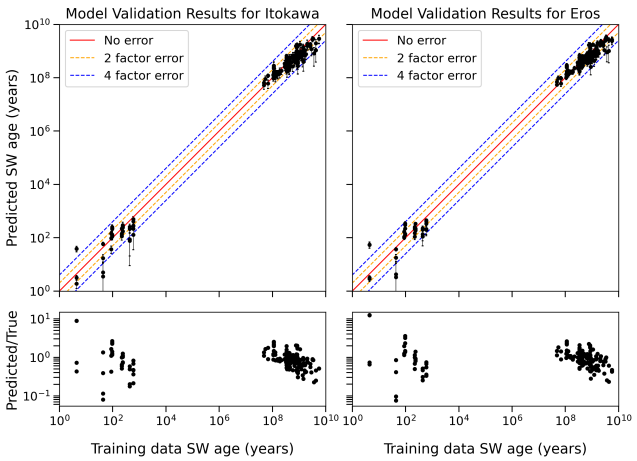

Figure 2. Top: scatter plot of the training and predicted values after k-fold cross validation for both Itokawa and Eros. The red line represents an exact match, the orange line a 2-factor error, and the blue line a 4-factor error. Bottom: the ratio between the predicted SW age and the training data SW age.

regressor (GBR), K-nearest neighbor (KNN) regressor, extra-tree regressor (ETR), and random forest regressor (RFR). To optimize overall performance, each model was assigned a specific weight using Scikit-learn's VotingRegressor ($w_{\rm CNN}$, $w_{\rm GBR}$, $w_{\rm KNN}$, $w_{\rm ETR}$, and $w_{\rm RFR}$). In this study, the Ensemble model was retrained with updated parameters, including modifications to the CNN architecture and its hyperparameters, as detailed in Table A1. These hyperparameters were selected through a random search strategy, guided by validation performance. Based on this optimization, new weights were assigned: $w_{\rm CNN} = 4$, $w_{\rm GBR} = 4$, $w_{\rm KNN} = 1$, $w_{\rm ETR} = 5$, and $w_{\rm RFR} = 1$. Model evaluation was performed using 5-fold cross validation to ensure robustness and generalizability.

The top row of the Figure 2 presents the results of the model validation for Itokawa and Eros spectral grids using the validation datasets. In both plots, the horizontal axis represents the training data SW age in years, while the vertical axis represents the model-predicted SW age in years. As the models were trained on a logarithmic scale, the factor errors of 2 and 4 were calculated, corresponding to the diagonal reference lines in the plots. Each data point represents the average prediction obtained across 30 iterations, with vertical error bars indicating the standard deviation. The diagonal lines act as reference benchmarks, illustrating the degree of agreement between predicted and actual SW ages.

The coefficient of determination (R^2) values are 0.985 for the Itokawa model and 0.986 for the Eros model. Based on the R^2 values, both models produce an acceptable fit, capturing the overall trend in SW. The bottom row of the Figure 2 presents the ratio between the predicted SW age and the training data SW age. There are several data points that deviate from the no-error line by more than a factor of 4 at exposure ages below 50 yr. These correspond to H^+ irradiated OL samples. Because our analysis primarily considers OL–OPX mixtures and OC samples for asteroid SW age determination on S-type asteroids, and because the predicted exposure ages for these materials are generally greater than 1000 yr, the effect of this deviation on asteroid data is negligible.

Moreover, we evaluated the model performance using three additional matrices: root-mean-square error (RMSE), the 90th percentile error, and the mean bias. We calculated the bias (3), and the values are summarized in the Table 2. We calculated these metrics for five distinct data ranges: 1–10^2 yr, 10^2–10^3 yr, 10^7–10^8 yr, 10^8–10^9 yr, and 10^9–10^{10} yr.

$$bias = \log_{10}(t_{\rm predicted}) - \log_{10}(t_{\rm true}), \quad (3)$$

where $\log_{10}(t_{\rm predicted})$ is the predicted SW age and $\log_{10}(t_{\rm true})$ is the training data SW age.

Across all surfaces, the model yielded RMSE values of 0.296 and 0.286 for Itokawa and Eros, respectively, indicating consistent performance across both datasets. To characterize the distribution of larger deviations, we computed the 90th percentile of absolute prediction errors. This measure indicates that 90% of predictions lie within 1.26–2.95 log-years of the true age, depending on the SW age range, thereby highlighting the occurrence of occasional extreme errors that are less apparent in RMSE.

For both models, mean bias indicates slight overestimations and underestimations in certain age ranges. Positive values indicate overestimation, while negative values indicate underestimation. For young surfaces (10^0–10^2 yr), the model exhibits a slight overestimation (mean bias 0.15–0.20 log-years), whereas midage surfaces (10^2–10^3 yr) tend to be slightly underestimated (−0.21 to −0.24 log-years). For older surfaces ($>10^8$ yr), bias approaches zero, indicating minimal systematic error. Overall, in linear terms, these biases correspond to multiplicative factors of approximately 1.2–1.6. The model demonstrates consistent predictive capability across datasets, with minor systematic tendencies for young and midage surfaces and high accuracy for older surfaces. The systematic bias observed likely arises from a combination of data and model-related factors. Limitations in the training data can also contribute to bias. If the dataset underrepresents certain age ranges, compositions, or surface conditions, the model may generalize poorly, systematically under- or overestimating ages in these regimes.

3.2. SW Age Determination

As mentioned above, laboratory-simulated data were used as the input. The following method was applied to calibrate the simulated conditions to asteroid surface weathering at 1 au. We derived SW ages from the laboratory simulations using experimental fluences together with parameters representative of typical planetary environments, such as solar wind flux. For ion irradiation, the SW age is computed as

$$t_{\rm ion} = \frac{4F}{f_{\rm ion}}, \quad (4)$$

where $t_{\rm ion}$ is the SW age, F is the fluence of the ion particles used, and $f_{\rm ion}$ is the flux of solar photons at 1 au (K. Chrbolková et al. 2021). A factor of 4 was applied to approximate the object as a rotating sphere, considering the H^+ to He^+ ion ratio and the proton flux of approximately 2.9×10^8 ions cm^{-2} s^{-1} at 1 au (R. Schwenn 2000).

The energy delivered to an asteroid surface (A) by micrometeorite impacts is given by

$$A = \frac{1}{2} m v^2 f_{\rm particles}, \quad (5)$$

where m is the particle mass, v is the average impact velocity, and $f_{\rm particles}$ is the particle flux. Impact fluxes and velocities at 1 au were adopted from published models (e.g., E. Grun et al. 1991).

Table 2
Mean Bias, Percentile Factor Error, and RMSE for Two Models

SW Age		Number of Samples	Itokawa			Eros		
yr	$\log_{10}$ (yr)		RMSE $\log_{10}$ (yr)	90th Percentile	Mean bias $\log_{10}$ (yr)	RMSE $\log_{10}$ (yr)	90th Percentile	Mean Bias $\log_{10}$ (yr)
Overall	⋯	⋯	0.296	2.95	⋯	0.286	2.39	⋯
10^0–10^2	1–2	20	0.535	2.39	0.147	0.555	2.75	0.195
10^2–10^3	2–3	20	0.338	1.95	−0.237	0.293	1.61	−0.211
10^7–10^8	7–8	6	0.160	1.26	0.117	0.158	1.25	0.117
10^8–10^9	8–9	88	0.201	1.39	−0.031	0.183	1.37	0.011
10^9–10^{10}	9–10	34	0.286	1.55	−0.223	0.271	1.49	−0.198

In the laser experiments, the deposited energy density B is

$$B = \frac{E}{S}, \tag{6}$$

with E being the total delivered energy and S the laser spot area. The corresponding SW age simulated by laser irradiation is then

$$t_{\text{laser}} = \frac{B}{A}. \tag{7}$$

Using the model, as an output, we obtained two sets of SW age estimates for both Itokawa and Eros computed to the 1 au distance from the Sun. One set of SW ages assumes solar wind irradiation (H^+) as the dominant SW agent, and the other assumes micrometeorite impacts as the dominant agent. These ages were adjusted based on each asteroid's current heliocentric distance, using semimajor axes of 1.3 au for Itokawa and 1.4 au for Eros. Subsequently, we calculate the solar wind SW age t_{solar} and micrometeorite impact age t_{impact} using the following equations:

$$t_{\text{solar}} = t_{\text{ion}} \frac{d^2}{(1\ \text{au})^2}, \tag{8}$$

$$t_{\text{impact}} = t_{\text{laser}} \frac{A_{1\text{au}}}{A}, \tag{9}$$

where $A_{1\text{au}}$ is energy delivered to an asteroid surface at 1 au. Impact velocities at 1.3 and 1.4 au were obtained from the model developed by R. Jehn (2000). d is the distance from the Sun (semimajor axis). The solar wind ion flux decreases approximately with the square of the heliocentric distance (R. Schwenn 2000). All scripts used for these calculations are publicly available in the associated GitHub and Zenodo repositories.

To identify the dominant SW agent for each surface region, we referred to Figure 9 in L. Palamakumbure et al. (2025), which defines the solar wind saturation limits at these distances. The solar wind saturation thresholds are approximately 3 kyr for 1.3 au (Itokawa) and 3.6 kyr for 1.4 au (Eros). SW ages below this threshold indicate that the SW is dominated by the solar wind, and the SW age was taken from the corresponding solar wind age model, while SW ages above this threshold are interpreted as being primarily influenced by micrometeorite impacts and were therefore assigned from the micrometeorite age model.

To aid visualization, we generated 3D SW age maps of Itokawa and Eros. These maps show the distribution of SW ages across each asteroid. The 3D projection maps were generated using the ShapeViewer[6] software (J. B. Vincent 2018).

[6] https://www.comet-toolbox.com/shapeViewer.html

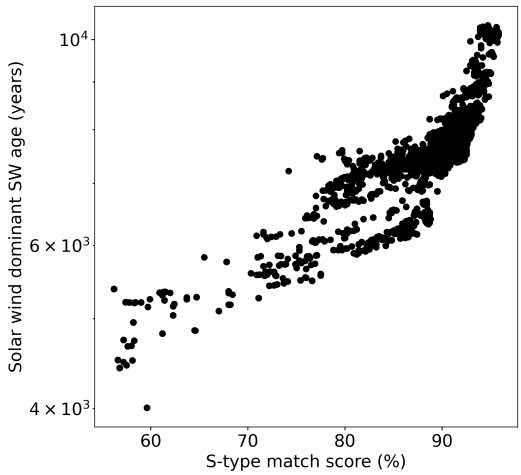

Figure 3. Distance-corrected solar wind dominant SW age of Eros plotted against the S-type match score by D. Korda et al. (2023).

4. Results

The results for the SW ages of Itokawa and Eros obtained from the model are presented in two sections as follows: (1) SW age estimation of Eros and (2) SW age estimation of Itokawa. In addition, our results are compared with surface composition and maturity analyses reported by D. Korda et al. (2023), who employed a machine learning–based approach.

4.1. Eros

In Figure 3, we plotted the distance-corrected solar wind dominant SW age of Eros against the S-type match score reported by D. Korda et al. (2023). Here, D. Korda et al. (2023) define the match score as the probability of individual taxonomic classes and as silicate composition as modal abundance in percent. The distance-corrected solar wind dominant SW age ranges from 4 to 10 kyr. S-type match score increases with SW age, and the SW age at every point is greater than 3.5 kyr, the solar wind saturation limit at 1.4 au (L. Palamakumbure et al. 2023). Hence, we assign distance-corrected micrometeorite-dominant SW ages for every point. Consequently, as shown in Figure 4, the surface of Eros is weathered dominantly by micrometeorite impacts with a mature surface, SW ages ranging from 0.5 to 2.8 Gyr. However, the resolution of the Eros dataset was notably lower than that of Itokawa, introducing greater uncertainty in the model's predictions for Eros.

In Figure 5, the silicate mineral proportions of Eros as determined by D. Korda et al. (2023) are plotted against the SW age. There is no significant correlation between OL

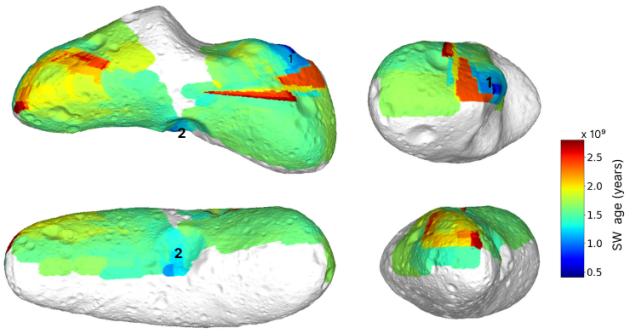

Figure 4. Prediction of the SW age on the Eros surface. The numbers are designated for fresh areas.

abundance and SW age. Large variability across the entire age range suggests that OL abundance remains relatively stable over time. OPX abundance shows a moderate increase with SW age. For mineral chemistry, both fayalite (Fa) and ferrosilite (Fs) number exhibit negative correlations with SW age. This suggests a progressive enrichment in magnesium over time. This trend is consistent with SW processes that preferentially alter Fe-rich mineral components. Specifically, these processes may lead to the formation of npFe^0, which results from the reduction of Fe-bearing silicates, and the silicates become relatively more Mg-rich, explaining the compositional shift observed on older surfaces.

4.2. Itokawa

In Figure 6, we plotted the distance-corrected solar wind dominant SW age against the S-type match score reported by D. Korda et al. (2023). The solar wind dominant SW age, corrected for heliocentric distance, ranges from 1.9 to 5.5 kyr, while the micrometeorite impact dominant SW age spans from 1 to 2.5 Gyr. The S-type score generally increases with solar wind dominant SW age, but unlike Eros, the data reveal two distinct clusters separated by around 3.25 kyr. The origin of these clusters remains unclear.

Figure 7 illustrates the distribution of SW ages dominated by solar wind and micrometeorite impacts. Although the solar wind saturation age at 1.3 au (identified by L. Palamakumbure et al. 2025) is approximately 3 kyr (marked by the red dashed line in Figure 6), the presence of two clusters and the gap in between complicates an accurate determination of micrometeorite impact SW ages above this threshold. This is discussed further in Section 5. Combining the solar wind and micrometeorite age predictions we assign solar wind–dominated SW ages to regions below the saturation line and classify regions above it as older than 3 kyr (Figure 8). Our modeling indicates that Itokawa's surface evolution is influenced by both solar wind irradiation and micrometeorite impacts.

In Figure 9, the chemical composition data derived from D. Korda et al. (2023) are plotted against the SW age. The abundance of OL shows a decreasing trend with increasing SW age, suggesting that OL may be sensitive to surface aging processes. In contrast, OPX abundance does not show a clear correlation with age. Similarly, the Fa number in OL and the Fs number in OPX exhibit no consistent relationship with SW age.

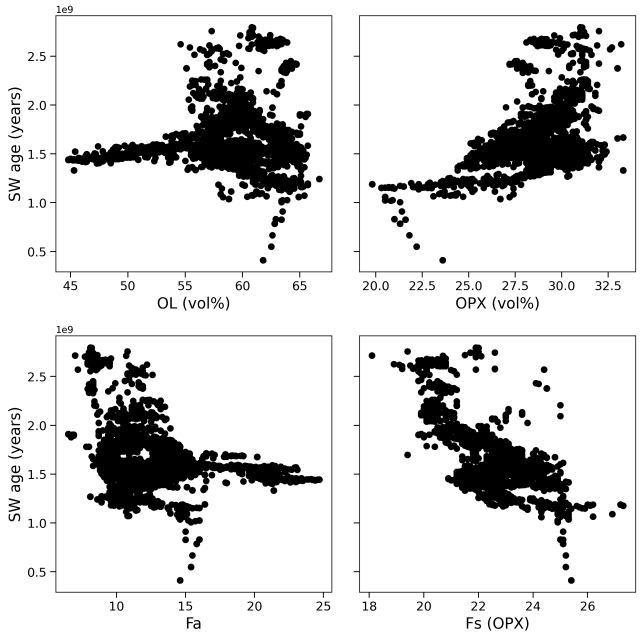

Figure 5. SW age of Eros plotted against the OL (vol%), OPX (vol%), Fa, and Fs (OPX) content by D. Korda et al. (2023).

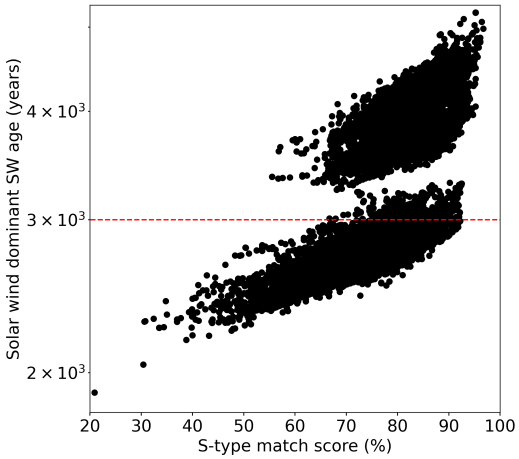

Figure 6. Distance-corrected solar wind dominant SW age of Itokawa plotted against the S-type match score by D. Korda et al. (2023).

5. Discussion

Our results provide valuable insights into the surface aging processes of two S-type asteroids, Itokawa and Eros, highlighting distinct evolutionary patterns shaped by different dominant SW agents and regolith dynamics. Itokawa exhibits young solar wind–dominated SW ages, with predicted values ranging from 1.9 to 5.2 kyr, whereas its micrometeorite impact–dominated SW ages are significantly older, spanning 1.25–2.5 Gyr. When the two SW-derived SW age estimates are combined, the younger regions cluster within 2–3 kyr, while the more mature regions exhibit SW ages exceeding 3 kyr. In contrast, Eros shows SW ages that are predominantly controlled by micrometeorite impacts, with predicted SW ages ranging from 0.4 to 2.8 Gyr at a heliocentric distance of 1.4 au.

When comparing the asteroid SW ages predicted by L. Palamakumbure et al. (2025) at 1.3 and 1.4 au, Itokawa's micrometeorite impact SW age range is narrower than the

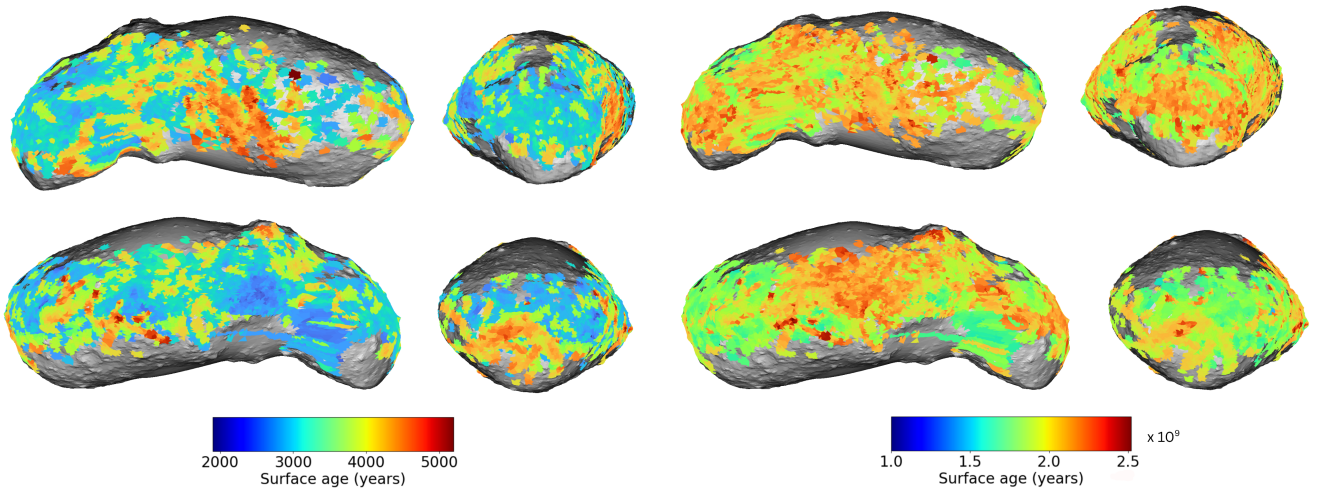

Figure 7. Prediction of the solar wind (left) and microimpact (right) SW age on the Itokawa.

model's full prediction range. In Figure 10, we compared the Itokawa and Eros SW age ranges with the other asteroid ages predicted by L. Palamakumbure et al. (2025). The SW age range of Itokawa aligns well with that of other asteroids with similar solar distances and diameters, but Eros exhibits a broader distribution.

5.1. SW Age of Eros

The mature SW ages estimated for Eros, ranging from 0.4 to 2.8 Gyr, agree well with previous spectral studies and surface morphology analyses (B. E. Clark et al. 2001; F. E. DeMeo et al. 2009; M. Mahlke et al. 2022; D. Korda et al. 2023), supporting the interpretation of a geologically evolved and space-weathered body. Notably, C. R. Chapman et al. (2002) proposed that Eros originated from a catastrophic cratering event in the asteroid belt that occurred approximately 2 Gyr ago. Further, their study concludes that Eros is unlikely to have been an exterior fragment, and all the surface features are presumed to have formed after the breakup event from the parent body. This aligns with the SW ages produced by our model, with the maximum SW age approximately 2.8 Gyr.

The surface composition of Eros is generally consistent with L/LL chondritic material (C. N. Foley et al. 2006; P. N. Peplowski et al. 2015). However, mean surface measurements of OL and OPX abundance and Fa and Fs number reported by D. Korda et al. (2023) fall below the values typically normalized for L/LL-chondrites. For comparison, L-chondrites exhibit Fa number of 23–24 and Fs number of 20.2–21, with OL comprising about 60.5 vol%; LL-chondrites show Fa number of 28.9–29.9, Fs number of 23.6–24.5, and OL abundances near 66 vol% (T. J. McCoy et al. 2001; P. Wang et al. 2022). D. Korda et al. (2023) attribute this to SW effects. The apparent overall reduced OL abundance derived from reflectance spectra by D. Korda et al. (2023) and its weak correlation with our SW age values suggest that the observed decrease in OL abundance may be related to amorphization caused by early solar wind–dominated SW, which is saturated on Eros. In contrast, we observe a correlation in declining Fa and Fs number with our SW ages, indicative of a still ongoing progressive surface enrichment in Mg-rich silicates caused by reduction of Fe^{2+} into nanophase metallic iron ($npFe^{0}$) typical of microimpact-dominated SW environments (e.g., K. Chrbolková et al. 2022). These changes point to a mature SW history for Eros, consistent with its older SW ages and ongoing micrometeorite-dominated SW regime. Overall, our findings reinforce the view of Eros as a geologically mature S-type asteroid, with surface evolution primarily driven by micrometeorite bombardment and gradual SW.

Despite this, there are two regions relatively young than the surrounding ones identified on Eros that are marked as (1) and (2) in Figure 4, with region (1) corresponding to the northwest of Shoemaker crater and region (2) corresponding to the crater Psyche, previously characterized by J. Veverka et al. (2000) and P. C. Thomas et al. (2002). However, estimating the SW age of smaller craters remains challenging due to the limited spatial resolution of the available data.

Although our SW age map lacks data for the center of the Shoemaker crater, the northwestern rim appears relatively younger than region (2), the Psyche crater. This observation is consistent with the findings of P. C. Thomas et al. (2002), who noted morphological freshness in that area. D. Korda et al. (2023) also reported elevated OL and reduced OPX abundances in the same region. They attributed this to the differential response of OL and OPX to SW, with OL's spectral features attenuating more rapidly, making it a sensitive indicator of surface freshness. However, J. Bell et al. (2002) identified this area as more weathered, citing a local minimum in the 1000 nm absorption band depth. This apparent contradiction may reflect the complex interplay between compositional heterogeneity, regolith mixing, and varying degrees of SW exposure across small spatial scales. It also highlights the limitations of relying on a single spectral parameter to assess surface maturity.

The Psyche crater exhibits a relatively young surface compared to the surrounding regions. M. S. Robinson et al. (2002) described Psyche as having a fresh morphology among Eros's craters, although its southern edge is intersected by four smaller (approximately 1 km) craters. Our model supports this, showing a relatively fresh surface in region (2), particularly toward its southern margin. These smaller impacts likely excavated deeper, less weathered material, locally resetting the surface exposure age.

This interpretation is further supported by the increased OL abundance in region (2), as reported by D. Korda et al. (2023). Since freshly exposed surfaces tend to exhibit lower spectral maturity, the elevated OL abundance aligns with a younger,

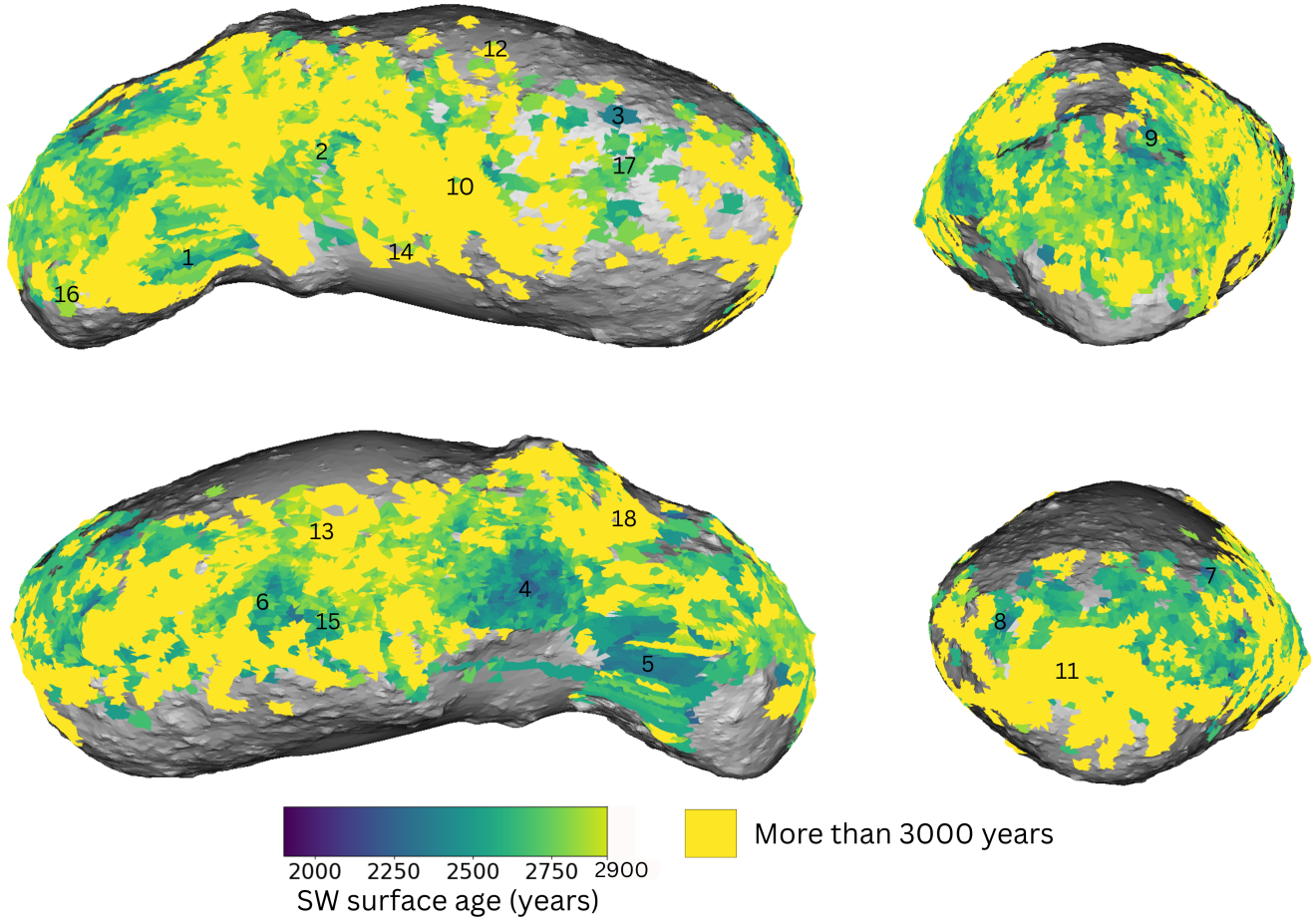

Figure 8. Combined prediction of the SW age on the Itokawa. The numbers are designated for fresh and mature areas.

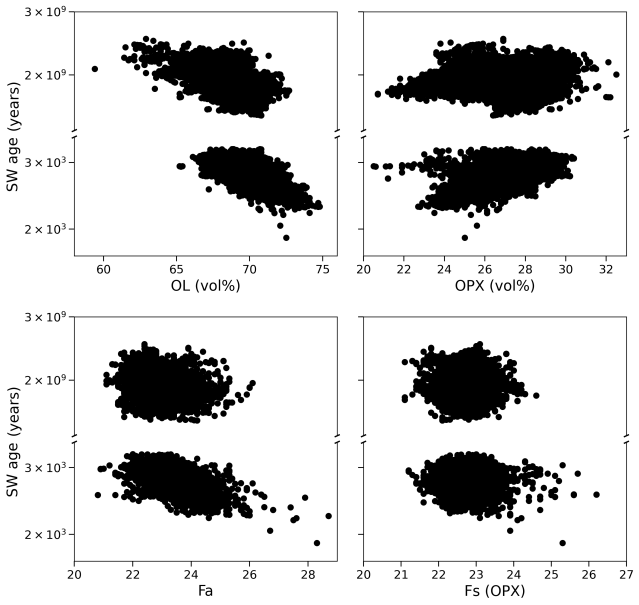

Figure 9. SW age of Itokawa plotted against the OL (vol%), OPX (vol%), Fa, and Fs (OPX) by D. Korda et al. (2023).

less weathered regolith. Over time, SW processes progressively obscure these features, reducing OL spectral contrast and increasing overall maturity. The presence of younger regions, such as the crater in regions (1) and (2), provides valuable information on the resurfacing processes and the timescales over which spectral maturation occurs.

5.2. SW Age of Itokawa

Previous studies have suggested that Itokawa's surface is young, with minor-to-moderate exposure ages inferred from regolith morphology, spectral maturity, and particle analyses (J. Saito et al. 2006; M. Ishiguro et al. 2007; S. C. Koga et al. 2018; S. Jin & M. Ishiguro 2022; D. Korda et al. 2023). These interpretations are largely consistent with our model results (see Figure 11), which indicate that Itokawa's surface comprises young terrains, with estimated ages ranging from approximately 1.9 to 3 kyr. Furthermore, our SW age distribution (Figure 8) shows strong spatial correlation with the low-SW regions identified by S. C. Koga et al. (2018) using observed color angle analysis of AMICA images. Our model prediction for the sample collection site, an estimated SW age of approximately 3 kyr, aligns well with findings from returned sample analyses. Studies by T. Noguchi et al. (2014) and T. Matsumoto et al. (2015, 2016) concluded that the SW rims observed on the grains were primarily formed by solar wind irradiation, with a weathering timescale on the order of 10^3–10^4 yr. Similarly, S. Jin & M. Ishiguro (2022) derived the SW timescale of approximately 10^3 yr based on the size distribution of bright mottles on boulder surfaces.

Our model supports the findings of K. D. Burgess & R. M. Stroud (2021), who reported varying degrees of SW

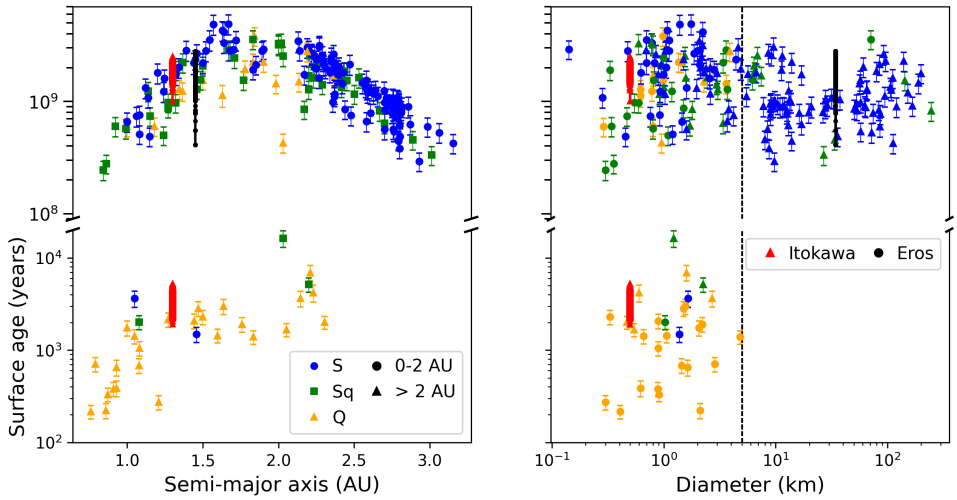

Figure 10. SW age of Itokawa and Eros with the SW ages of asteroids predicted by L. Palamakumbure et al. (2025) with semimajor axis and size. Note that for Eros, only the micrometeorite-dominant age is plotted because it is above the solar wind saturation limit.

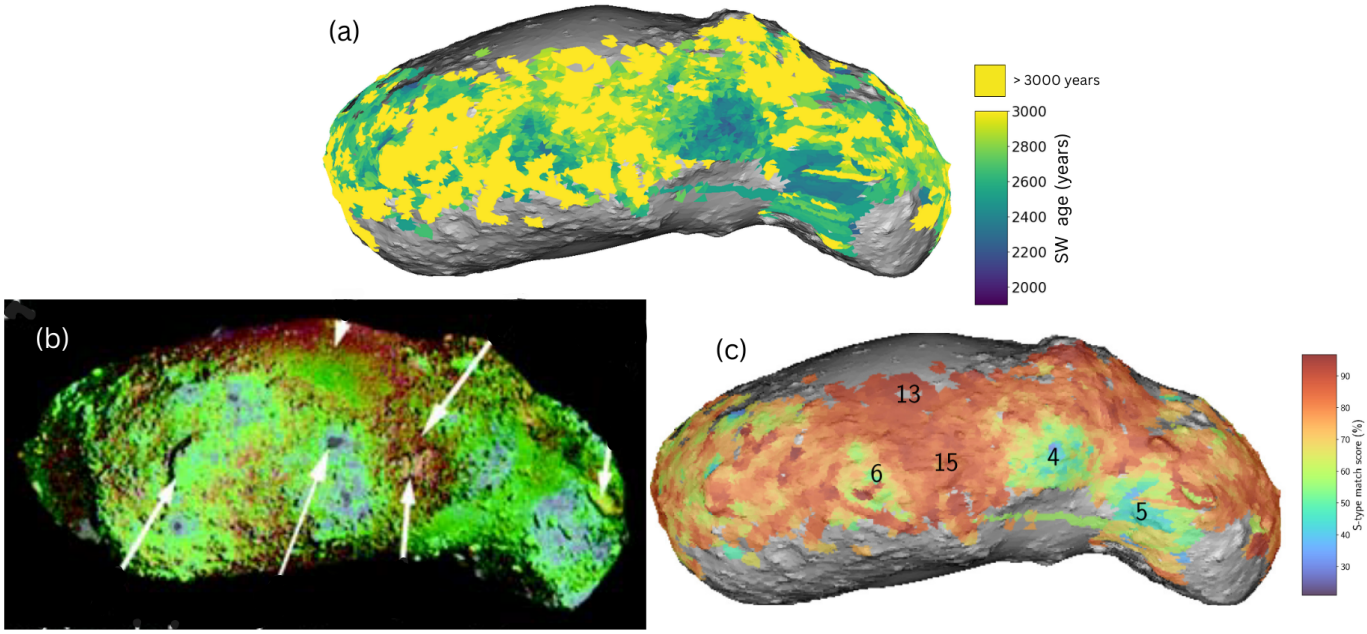

Figure 11. SW age of Itokawa and other studies. (a) This study, (b) D. Korda et al. (2023), and (c) M. Ishiguro et al. (2007)

across two sampling sites 100 m apart, within the same region of Itokawa. These observations highlight the spatial heterogeneity of SW on Itokawa, even at relatively small scales. This heterogeneity is reflected in our SW age map, which reveals the coexistence of freshly exposed and more weathered terrains within localized areas. Such variability is likely driven by dynamic surface processes, including micrometeorite impacts, seismic shaking, and regolith movement. Further supporting our model, M. S. Thompson et al. (2014b) provided evidence that Itokawa has undergone a complex processing history involving both solar wind irradiation and micrometeorite bombardment. These combined influences contribute to the observed diversity in SW and SW age across the asteroid.

As mentioned in Section 4.2, our study also identifies significantly older surface regions on Itokawa, with distance-corrected micrometeorite-dominant SW age estimates exceeding 10^9 yr, predominantly attributed to micrometeorite impact–induced weathering. Radioisotope dating of returned Itokawa samples by A. Tsuchiyama (2014) indicates that the asteroid originated from a parent body that formed approximately 4.5 billion years ago. This suggests that Itokawa's regolith comprises both freshly exposed material and ancient lithologies inherited from its precursor. These older SW age estimates likely represent remnants of the parent body's original surface, intermittently exposed due to resurfacing processes. Itokawa is hypothesized to have experienced frequent resurfacing events, potentially driven by regolith migration (H. Miyamoto et al. 2007), tidal interactions during close planetary encounters (R. P. Binzel et al. 2010), or seismic shaking induced by impacts (A. Tsuchiyama et al. 2011). While solar wind irradiation dominates the early stages of SW, micrometeorite impacts appear to play a key role in longer-term evolution by excavating and mixing deeper, older materials. The coexistence of both young and ancient terrains underscores the dynamic and

Table 3
Approximate SW Ages of the Craters and Regions on Itokawa

Name	ID	Type	Latitude	Longitude	SW Age (yr)
Kamoi	6	Crater	6	244	$(2 \pm 0.71) \times 10^3$
Laurel	8	Crater	1	162	$(2 \pm 0.73) \times 10^3$
Miyabaru	9	Crater	8	8	$(2 \pm 0.66) \times 10^3$
Komaba	10	Crater	−10	102	$\geqslant 3 \times 10^3$
Arcoon	11	Region	−10	175	$\geqslant 3 \times 10^3$
Uchinoura	12	Region	40	112	$\geqslant 3 \times 10^3$
Fuchinobe	13	Crater	34	269	$(3 \pm 0.88) \times 10^3$
Ohsumi	15	Region	−2	275	$(1 \pm 0.59) \times 10^9$
Catalina	16	Crater	−17	14	$(2 \pm 0.77) \times 10^3$
LINEAR	17	Region	0	128	$(2 \pm 0.80) \times 10^3$
Yoshinobu	18	Region	25	348	$\geqslant 3 \times 10^3$

Note. Uncertainties represent one standard deviation. Ages with "⩾" indicate lower limits due to limited resurfacing.

heterogeneous nature of Itokawa's surface history. Table 3 gives the approximate SW ages of the craters and places on Itokawa approved by the International Astronomical Union.

In addition to the regions mentioned in the Table 3, we have recognized five new, fresh areas, labeled (1) through (5) in Figure 8. Among these, areas (1), (3), and (5) are located on regions with higher local slopes, consistent with the topographic features described by R. A. Werner & D. J. Scheeres (1997) and A. F. Cheng et al. (2012). Areas (4) and (5) are situated in rough terrains on either side of the neck, characterized by locally elevated gravitational potential, which promotes resurfacing processes.

The remaining younger areas mentioned in the Table 3 are associated with impact craters, including Kamoi (6), Laurel (8), Miyabaru (9), Fuchinobe (13), and Catalina (16). In contrast, all mature regions, Arcoon (11), Uchinoura (12), Ohsumi (15), and Yoshinobu (18), are located in relatively low-potential zones, suggesting that these areas may have experienced material accumulation over time due to gravitational settling. Our model also indicates a mature SW age for the Komaba crater (10), while the LINEAR region (17) exhibits a significantly younger age, further supporting the spatial variability in surface evolution across Itokawa. Finally, it is important to note that the predictive model used in this study does not resolve SW ages between 10^4 and 10^7 yr. This limitation may lead to overestimation of some micrometeorite-dominant SW ages, as intermediate-aged terrains are mapped directly into the oldest SW age class. Nevertheless, the dual presence of young and old surface components on Itokawa underscores the complex interplay between solar wind weathering, micrometeorite impacts, and regolith evolution over geological timescales.

When it comes to silicate composition, Itokawa is composed of LL chondritic material (Fa of 28.9–29.9, Fs of 23.6–24.5, and OL abundances near 66 vol%), as established by T. Nakamura et al. (2011), A. Tsuchiyama et al. (2011), and A. Tsuchiyama (2014). D. Korda et al. (2023) applied a machine learning approach to estimate its surface composition, which we compared with SW ages derived from our model to explore potential correlations between SW and mineralogical changes (see Figure 9). Our analysis reveals an apparent decrease in OL abundance with increasing SW age, while the Fa number remains constant. This points to ongoing SW with progressive OL amorphization and apparent OL depletion in reflectance spectra but limited Fe^{2+} reduction into nanophase iron ($npFe^0$), as seen in Eros with older SW ages. This observation aligns with findings by K. Chrbolková et al. (2022), who demonstrated that solar wind irradiation leads to vesicle formation and partial amorphization in OL, while micrometeorite impacts produce fully amorphous layers with extensive Fe^{2+} reduction into nanophase iron ($npFe^0$).

Interestingly, K. Chrbolková et al. (2022) also reported that OPX develops a thick amorphous layer under micrometeorite bombardment. However, our results show no clear correlation between OPX abundance and SW age. Moreover, the lack of correlation in Fa and Fs number further supports the hypothesis that mineral chemistry remains largely stable over time, even as physical and structural changes occur due to SW.

The contrasting SW ages and dominant SW processes observed between Itokawa and Eros underscore the critical influence of asteroid size, orbital dynamics, and regolith properties in governing surface evolution. Smaller asteroids like Itokawa are dynamically active and undergo frequent resurfacing events, resulting in a patchwork of young and mature terrains. In contrast, larger bodies such as Eros tend to preserve ancient surface features, with limited evidence of recent regolith turnover.

Itokawa's contact binary structure may further contribute to its dynamic surface history. Reshaping events associated with its formation or subsequent tidal interactions could explain the presence of localized regions with significantly younger SW ages. These findings highlight the importance of internal structure and collisional history in modulating the surface renewal processes on small bodies.

5.3. Source of Uncertainties

Despite the model bias mentioned in Section 3.1, the SW ages derived from spectral trends should be interpreted as exposure times under present-day interplanetary conditions rather than as true chronological surface ages. Asteroid surfaces evolve dynamically, and processes such as regolith gardening, impacts, planetary encounters, and micrometeorite bombardment can partially reset SW signatures by exposing fresher material (e.g., C. R. Chapman 1996; F. E. DeMeo et al. 2023). These effects, together with surface heterogeneities, can lead to deviations between the derived SW age and the actual exposure history, without undermining the validity of SW age as a location-dependent weathering metric.

Furthermore, P. Michel & M. Yoshikawa (2006) estimated the source region of Itokawa by using the near-Earth object population model of W. F. Bottke et al. (2002), which quantifies the contributions of different dynamical sources to the unbiased orbital distribution of near-Earth objects. Their analysis indicates that Itokawa has approximately 64% probability of originating in the inner main belt via the ν_6 resonance, approximately 35% probability of coming from the Mars crosser population, and only approximately 1% likelihood of originating in the Hungaria group. These results, together with Itokawa's S-type taxonomy, strongly suggest an origin in the inner main belt.

In this context, the micrometeorite-dominated SW ages we report for Itokawa and Eros must be interpreted with caution. These ages rely on a correction based solely on the present semimajor axes of the two bodies (1.3 au for Itokawa, 1.4 au for Eros) and therefore do not account for their earlier

residence in the main belt or for the complex, chaotic orbital evolution that typically characterizes migration into near-Earth space. Heliocentric distance corrections for exposure ages depend strongly on the parameters used, such as particle flux values extracted from models. Moreover, these models are highly reliant on interplanetary environmental conditions derived from flux models, which themselves carry uncertainties. Because micrometeorite fluxes, impact velocities, and solar wind exposure vary substantially with heliocentric distance, the true cumulative surface exposure histories of these bodies over $\geqslant 10^8$ yr are unlikely to be captured accurately using their current orbits alone. Moreover, the migration pathways and dynamical lifetimes of near-Earth asteroids, typically on the order of 10^7 yr, are themselves uncertain, introducing additional, difficult-to-quantify systematic errors. Consequently, the micrometeorite-dominated ages should be regarded as approximate upper limits rather than precise measures of absolute surface exposure.

Previous studies have observed grain-size-dependent spectral slope variations in fresh materials, but these effects were often treated as secondary to interpretations focused on SW. E. M. MACLennan et al. (2024) demonstrate that grain size alone can produce spectral slope changes comparable to those caused by irradiation, highlighting an inherent ambiguity in slope-based weathering interpretations. Much of the earlier work relied on fixed grain sizes or mixed sample preparations and therefore did not fully acknowledge this degeneracy.

While laboratory studies show that grain size can induce spectral slope variations comparable to those produced by SW, this ambiguity arises primarily when low-dimensional spectral parameters, such as slope or band depth, are considered in isolation. In contrast, our machine learning approach utilizes the full reflectance spectrum in the near-infrared and visible region, samples with various grain sizes, enabling the model to learn higher-order spectral features associated with SW that are not reproduced by grain size effects alone. Several studies (e.g., K. Chrbolková et al. 2021; L. Palamakumbure et al. 2023) show that the SW influences specific spectral regions with different intensity, and thus a robust code should distinguish these from grain size effects. Grain size influences band shape, width, and continuum curvature, and these effects are therefore inherently encoded in the spectral input and can be implicitly accounted for during training. The validity of this methodology is further supported by the agreement between model-predicted weathering ages and exposure ages derived from Hayabusa samples returned from asteroid Itokawa.

Overall, our results also demonstrate the utility of machine learning in disentangling the complex interplay between spectral alteration and exposure history. However, it is important to acknowledge the limitations and uncertainties imposed by the abovementioned factors. The SW ages reported here should be regarded as model-dependent effective ages, likely representing lower limits on the time since the last significant resurfacing event rather than precise absolute ages. Furthermore, the spatial resolution of the Eros dataset is notably lower than that of Itokawa, which may obscure finer-scale heterogeneities in both SW age and composition.

Future missions equipped with higher-resolution instruments and in situ analysis capabilities will be essential to resolve these uncertainties. Such missions could validate current models, refine our understanding of SW processes and provide deeper insights into the evolutionary pathways of small solar system bodies.

6. Conclusions

This study offers a comparative analysis of the surface evolution of two S-type asteroids, Itokawa and Eros, highlighting how differences in size, structure, and dynamical history influence their respective SW regimes. Itokawa exhibits a highly dynamic and heterogeneous surface, with ages ranging from a few thousand to over a billion years. Both solar wind irradiation and micrometeorite-driven processes are present on Itokawa with ongoing OL amorphization and little Fe^{2+} reduction into nanophase iron ($npFe^0$). In contrast, Eros presents a more uniform and geologically mature surface, with ages between 0.4 and 2.8 billion years having micrometeorite impacts as the dominant SW agent with ongoing Fe^{2+} reduction into nanophase iron ($npFe^0$). Its larger size and structural stability have preserved ancient terrains, with only localized resurfacing, such as near the Shoemaker and Psyche craters, likely caused by smaller impact events. The contrasting surface characteristics of Itokawa and Eros underscore the critical role of asteroid size, internal structure, and orbital dynamics in governing surface evolution. Itokawa's contact binary structure and dynamic environment foster frequent rejuvenation, while Eros's more stable form supports long-term accumulation of SW effects.

Our application of machine learning has proven effective in resolving the complex relationships between spectral maturity, SW age, and composition. However, surface exposure ages derived from spectral SW trends carry inherent uncertainties due to resurfacing, regolith gardening, and orbital evolution. Our machine learning model demonstrates consistent predictive capability across datasets, with minor systematic tendencies: slight underestimation for young surfaces between 10^2 and 10^3 yr (factor of 1.2–1.6) and slight overestimation for midage surfaces, while older surfaces show minimal bias. These systematic biases likely reflect a combination of training data limitations and model-related factors. It is important to note that the resulting SW ages should be interpreted as model-dependent effective ages, likely representing lower limits since the last major resurfacing. Moreover, limitations in spatial resolution, particularly for Eros, highlight the need for future missions equipped with high-resolution instruments and in situ analysis capabilities. Such missions will be essential for validating current models, resolving fine-scale heterogeneity, and deepening our understanding of the evolutionary pathways of small solar system bodies. Together, these findings provide valuable insights into the mechanisms of SW and regolith evolution, offering a robust framework for interpreting data from ongoing and future asteroid exploration missions.

Acknowledgments

This work was supported by the Doctoral program of the University of Helsinki and the institutional support RVO 67985831 of the Institute of Geology of the Czech Academy of Science. The open access publication cost was funded by Helsinki University Library. We utilized data stored in the RELAB Spectral Database operated by Brown University and the C-Tape database operated by the University of Winnipeg. We also would like to extend our thanks to Rosario Brunetto and Zuzana Kaňuchová for providing laboratory reflectance data. This research has made use of scientific software *shapeViewer* (https://www.comet-toolbox.com/), NASA's SmallBody Database Lookup and the AsteroidFamiliesPortal (Bojan Novaković, David Vokrouhlický, Federica Spoto and

David Nesvorný: Asteroid Families: properties, recent advances and future opportunities 2022, Celest Mech Dyn Astro, 134, id. 34), and NASA's Astrophysics Data System Bibliographic Services. The authors would like to thank the anonymous referees for the valuable comments and suggestions, which greatly improved the quality of the paper.

Data Availability

The Python scripts and datasets, including all the sample spectra we used in this study, together with metadata, can be downloaded from GitHub repository https://github.com/Lakshika1990/Itokawa-and-Eros-surface-age-prediction.git.

Appendix
Hyperparameters for the CNN

In this Appendix, we provide details of the updated CNN architecture and its hyperparameters, as summarized in Table A1.

Table A1
Hyperparameters for the CNN Model

Property	Selected Value	Random Parameters
Network type	Convolutional	⋯
# hidden conv. layers	2	⋯
# filters in conv. layers	32, 32	16, 32, 64
Filter sizes	3, 2	2, 3, 4
Padding	same	⋯
Activation function	ReLU	ReLU, ELU, linear
Output nodes	1	⋯
Training algorithm	Adam	⋯
Batch size	32	16, 32, 64
Learning rate	0.001	0.01, 0.001
Maximum number of epochs	200	⋯

Note. Random parameters indicate the set of values tested for hyperparameter optimization. Dashes indicate fixed properties.

ORCID iDs

Lakshika Palamakumbure https://orcid.org/0000-0002-6811-4093
David Korda https://orcid.org/0000-0002-4227-251X
Tomáš Kohout https://orcid.org/0000-0003-4458-3650

References

Abe, M., Takagi, Y., Abe, S., & Kitazato, K. 2011, Hayabusa NIRS Calibrated Spectra v1.0, NASA Planetary Data System, id. HAY-A-NIRS-3-NIRSCAL-V1.0
Bell, J., Izenberg, N., Lucey, P., et al. 2002, Near-IR Reflectance Spectroscopy of 433 Eros from the NIS Instrument on the NEAR Mission: I. Low Phase Angle Observations, Icar, 155, 119
Binzel, R. P., Morbidelli, A., Merouane, S., et al. 2010, Earth Encounters as the Origin of Fresh Surfaces On Near-earth Asteroids, Natur, 463, 331
Binzel, R. P., Rivkin, A. S., Stuart, J. S., et al. 2004, Observed Spectral Properties of Near-earth Objects: Results for Population Distribution, Source Regions, and Space Weathering Processes, Icar, 170, 259
Bottke, W. F., Morbidelli, A., Jedicke, R., et al. 2002, Debiased Orbital and Absolute Magnitude Distribution of the Near-earth Objects, Icar, 156, 399
Brunetto, R., Romano, F., Blanco, A., et al. 2006, Space Weathering of Silicates Simulated by Nanosecond Pulse UV Excimer Laser, Icar, 180, 546
Burgess, K. D., & Stroud, R. M. 2021, Comparison of Space Weathering Features in Three Particles from Itokawa, M&PS, 56, 1109
Chapman, C. R. 1996, S-type Asteroids, Ordinary Chondrites, and Space Weathering: The Evidence from Galileo's Fly-by of Gaspra and Ida. Meteorit., M&PS, 31, 699
Chapman, C. R. 2004, Space Weathering of Asteroid Surfaces, AREPS, 32, 539
Chapman, C. R., Merline, W. J., Thomas, P. C., et al. 2002, Impact History of Eros: Craters and Boulders, Icar, 155, 104
Cheng, A. F. 1997, Near Earth Asteroid Rendezvous: Mission Overview, SSRv, 82, 3
Cheng, A. F., Barnouin, O. S., Ernst, C. M., & Kahn, E. G. 2012, Efficient Calculation of Effective Potential and Gravity on Small Bodies, LPICo, 1667, 6447
Chrbolková, K., Brunetto, R., Ďurech, J., et al. 2021, Comparison of Space Weathering Spectral Changes Induced by Solar Wind and Micrometeoroid Impacts Using ion- and Femtosecond-laser-irradiated Olivine and Pyroxene, A&A, 654, A143
Chrbolková, K., Halodová, P., Kohout, T., et al. 2022, Sub-surface Alteration and Related Change in Reflectance Spectra of Space-weathered Materials, A&A, 665, A14
Clark, B. E., Lucey, P., Helfenstein, P., et al. 2001, Space Weathering on Eros: Constraints from Albedo and Spectral Measurements of Psyche Crater, M&PS, 36, 1617
DeMeo, F. E., Binzel, R. P., Slivan, S. M., & Bus, S. J. 2009, An Extension of the Bus Asteroid Taxonomy into the Near-infrared, Icar, 202, 160
DeMeo, F. E., & Carry, B. 2014, Solar System Evolution from Compositional Mapping of the Asteroid Belt, Natur, 505, 629
DeMeo, F. E., Marsset, M., Polishook, D., et al. 2023, Isolating the Mechanisms for Asteroid Surface Refreshing, Icar, 389, 115264
Demura, H., Kobayashi, S., Nemoto, E., et al. 2006, Pole and Global Shape of 25143 Itokawa, Sci, 312, 1347
Dunn, T. L., Burbine, T. H., Bottke, W. F., & Clark, J. P. 2013, Mineralogies and Source Regions of Near Earth Asteroids, LPSC, 1197, 44
Foley, C. N., Nittler, L. R., McCoy, T. J., et al. 2006, Minor Element Evidence that Asteroid 433 Eros is a Space-weathered Ordinary Chondrite Parent Body, Icar, 184, 338
Fujiwara, A., Kawaguchi, J., Yeomans, D. K., et al. 2006, The Rubble-pile Asteroid Itokawa as Observed by Hayabusa, Sci, 312, 1330
Grun, E., Fechtig, H., Hanner, M. S., et al. 1991, In Situ Exploration of Dust in the Solar System and Initial Results from the Galileo Dust Detector (Invited Review), ASSL, 173, 21
Hiroi, T., Abe, M., Kitazato, K., et al. 2006, Developing Space Weathering on the Asteroid 25143 Itokawa, Natur, 443, 56
Ishiguro, M., Hiroi, T., Tholen, D. J., et al. 2007, Global Mapping of the Degree of Space Weathering on Asteroid 25143 Itokawa by Hayabusa/AMICA Observations, M&PS, 42, 1791
Jedicke, R., Nesvorný, D., & Whiteley, R. 2004, An Age–colour Relationship for Main-belt S-complex Asteroids, Natur, 429, 275
Jehn, R. 2000, An Analytical Model to Predict the Particle Flux on Spacecraft in the Solar System, P&SS, 48, 1429
Jin, S., & Ishiguro, M. 2022, Estimation of the Space Weathering Timescale on (25143) Itokawa: Implications on Its Rejuvenation Process, A&A, 667, A93
Kanuchova, Z., Brunetto, R., Fulvio, D., & Strazzulla, G. 2015, Near-ultraviolet Bluing After Space Weathering of Silicates and Meteorites, Icar, 258, 289
Kawaguchi, J., Uesugi, K., & Fujiwara, A. 2003, The MUSES-C Mission for the Sample and Return—its Technology Development Status and Readiness, AcAau, 52, 117
Keller, L. P., & Berger, E. L. 2014, A Transmission Electron Microscope Investigation of Space Weathering Effects in Hayabusa Samples, LPSC, 45, 1935
Koga, S. C., Sugita, S., Kamata, S., et al. 2018, Spectral Decomposition of Asteroid Itokawa Based on Principal Component Analysis, Icar, 299, 386
Kohout, T., Penttilä, A., Mann, P., et al. 2020, Distinguishing between Shock-darkening and Space-weathering Trends in Ordinary Chondrite Reflectance Spectra, PSJ, 1, 37
Korda, D., Kohout, T., Flanderová, K., Vincent, J.-B., & Penttilä, A. 2023, 433) Eros and (25143) Itokawa Surface Properties from Reflectance Spectra, A&A, 675, A50
Kracher, A., & Sears, D. W. 2005, Space Weathering and the Low Sulfur Abundance of Eros, Icar, 174, 36
MACLennan, E. M., Emery, J. P., Lucas, M. P., MCClure, L. M., & Lindsay, S. S. 2024, Space Weathering, Grain Size, and Metamorphic

Heating Effects on Ordinary Chondrite Spectral Reflectance Parameters, MAPS, 59, 1329
Mahlke, M., Carry, B., & Mattei, P. A. 2022, Asteroid Taxonomy from Cluster Analysis of Spectrometry and Albedo, A&A, 665, A26
Marchi, S., Brunetto, R., Magrin, S., Lazzarin, M., & Gandolfi, D. 2005, Space Weathering of Near-earth and Main Belt Silicate-rich Asteroids: Observations and Ion Irradiation Experiments, A&A, 443, 769
Matsumoto, T., Tsuchiyama, A., Miyake, A., et al. 2015, Surface and Internal Structures of a Space-weathered Rim of an Itokawa Regolith Particle, Icar, 257, 230
Matsumoto, T., Tsuchiyama, A., Uesugi, K., et al. 2016, Nanomorphology of Itokawa Regolith Particles: Application to Space-weathering Processes Affecting the Itokawa Asteroid, GeCoA, 187, 195
McCoy, T. J., Burbine, T. H., McFadden, L. A., et al. 2001, The Composition of 433 Eros: A Mineralogical-chemical Synthesis, M&PS, 36, 1661
McFadden, L. A., Wellnitz, D. D., Schnaubelt, M., et al. 2001, Mineralogical Interpretation of Reflectance Spectra of Eros from NEAR Near-infrared Spectrometer Low Phase Flyby, M&PS, 36, 1711
Michel, P., & Yoshikawa, M. 2006, Dynamical Origin of the Asteroid (25143) Itokawa: the Target of the Sample-return Hayabusa Space Mission, A&A, 449, 817
Miyamoto, H., Yano, H., Scheeres, D. J., et al. 2007, Regolith Migration and Sorting on Asteroid Itokawa, Sci, 316, 1011
Nakamura, T., Noguchi, T., Tanaka, M., et al. 2011, Itokawa Dust Particles: A Direct Link between S-Type Asteroids and Ordinary Chondrites, Sci, 333, 1113
Nesvorný, D., & Bottke, W. F. 2004, Detection of the Yarkovsky Effect for Main-belt Asteroids, Icar, 170, 324
Nesvorný, D., Jedicke, R., Whiteley, R. J., & Ivezić, Ž. 2005, Evidence for Asteroid Space Weathering from the Sloan Digital Sky Survey, Icar, 173, 132
Ni, C., & Zhang, H. 2025, Estimation of the Particle-size Distributions of Regolith on the Surface of (25143) Itokawa based on Near-infrared Reflectance Spectra, A&A, 699, A116
Nittler, L. R., Starr, R. D., Lim, L., et al. 2001, X-ray Fluorescence Measurements of the Surface Elemental Composition of Asteroid 433 Eros, M&PS, 36, 1673
Noguchi, T., Nakamura, T., Kimura, M., et al. 2011, Incipient Space Weathering Observed on the Surface of Itokawa Dust Particles, Sci, 333, 1121
Noguchi, T., Kimura, M., Hashimoto, T., et al. 2014, Space Weathered Rims Found on the Surfaces of the Itokawa Dust Particles, M&PS, 49, 188
Palamakumbure, L., Mizohata, K., Flanderová, K., et al. 2023, Simulation of Space Weathering on Asteroid Spectra through Hydrogen Ion Irradiation of Meteorites, PSJ, 4, 72
Palamakumbure, L., Syrjänen, S. A. I., Korda, D., Kohout, T., & Klami, A. 2025, Predicting the Surface Age of Chondritic S-type Asteroids Using the Space Weathering Features in Reflectance Spectra: Small Data Machine Learning, A&A, 699, A175
Peplowski, P. N., Bazell, D., Evans, L. G., et al. 2015, Hydrogen and Major Element Concentrations on 433 Eros: Evidence for an L- or LL-chondrite-like Surface Composition, MAPS, 50, 353
Robinson, M. S., Thomas, P. C., Veverka, J., Murchie, S. L., & Wilcox, B. B. 2002, The Geology of 433 Eros, M&PS, 37, 1651
Saito, J., Miyamoto, H., Nakamura, R., et al. 2006, Detailed Images of Asteroid 25143 Itokawa from Hayabusa, Sci, 312, 1341
Schwenn, R. 2000, Solar Wind: Global Properties, in Encyclopedia of Astronomy and Astrophysics, ed. P. Murdin, 2301 (IOP Publishing)
Strazzulla, G., Dotto, E., Binzel, R., et al. 2005, Spectral Alteration of the Meteorite Epinal (H5) Induced by Heavy Ion Irradiation: a Simulation of Space Weathering Effects on Near-earth asteroids, Icar, 174, 31
Thomas, P. C., Joseph, J., Carcich, B., et al. 2002, Eros: Shape, Topography, and Slope Processes, Icar, 155, 18
Thompson, M. S., Christoffersen, R., Zega, T. J., & Keller, L. P. 2014a, Nanoscale Analysis of Space-weathering Features in Soils from Itokawa, LPSC, 45, 2121
Thompson, M. S., Christoffersen, R., Zega, T. J., & Keller, L. P. 2014b, Microchemical and Structural Evidence for Space Weathering in Soils from Asteroid Itokawa, EP&S, 66, 89
Tsuchiyama, A. 2014, Asteroid Itokawa A Source of Ordinary Chondrites and A Laboratory for Surface Processes, Eleme, 10, 45
Tsuchiyama, A., Uesugi, M., Matsushima, T., et al. 2011, Three-dimensional Structure of Hayabusa Samples: Origin and Evolution of Itokawa Regolith, Sci, 333, 1125
Vernazza, P., Binzel, R. P., Rossi, A., Fulchignoni, M., & Birlan, M. 2009, Solar Wind as the Origin of Rapid Reddening of Asteroid Surfaces, Natur, 458, 993
Veverka, J., Robinson, M., Thomas, P., et al. 2000, NEAR at Eros: Imaging and Spectral Results, Sci, 289, 2088
Vincent, J. B. 2018, ShapeViewer, a Mapping Tool for the Morphological Analysis of Small Bodies and Mission Operations Planning, LPSC, 49, 1281
Wang, P., Cloutis, E., Zhang, Q., & Wu, Y. 2022, Quantitative Mineral Analysis of Ordinary Chondrites and Primitive Achondrites Using Reflectance Spectroscopy, JGRE, 127, e2022JE007571
Warren, J. W., Peacock, K., Darlington, E. H., et al. 1997, Near Infrared Spectrometer for the Near Earth Asteroid Rendezvous Mission, SSRv, 82, 101
Werner, R. A., & Scheeres, D. J. 1997, Exterior Gravitation of a Polyhedron Derived and Compared with Harmonic and Mascon Gravitation Representations of Asteroid 4769 Castalia, CeMDA, 65, 313
Willman, M., & Jedicke, R. 2011, Asteroid Age Distributions Determined by Space Weathering and Collisional Evolution Models, Icar, 211, 504
Willman, M., Jedicke, R., Moskovitz, N., et al. 2010, Using the Youngest Asteroid Clusters to Constrain the Space Weathering and Gardening Rate on S-complex Asteroids, Icar, 208, 758
Willman, M., Jedicke, R., Nesvorný, D., Vokrouhlický, D., & Mothé-Diniz, T. 2008, Redetermination of the Space Weathering Rate Using Spectra of Iannini Asteroid Family Members, Icar, 195, 663
Zhuang, Y., Zhang, H., Ma, P., et al. 2023, Visible and Near-infrared Reflectance Spectra of Igneous Rocks and their Powders, Icar, 391, 115346